

Computational hemodynamics framework for the analysis of cerebral aneurysms

Fernando Mut¹, Rainald Löhner¹, Aichi Chien², Satoshi Tateshima²,
Fernando Viñuela², Christopher Putman³ and Juan R. Cebal^{1,*},[†]

¹*Center for Computational Fluid Dynamics, Department of Computational and Data Sciences,
George Mason University, Fairfax, VA, U.S.A.*

²*UCLA Medical Center, University of California, Los Angeles, CA, U.S.A.*

³*Interventional Neuroradiology, Inova Fairfax Hospital, Falls Church, VA, U.S.A.*

SUMMARY

Assessing the risk of rupture of intracranial aneurysms is important for clinicians because the natural rupture risk can be exceeded by the small but significant risk carried by current treatments. To this end numerous investigators have used image-based computational fluid dynamics models to extract patient-specific hemodynamics information, but there is no consensus on which variables or hemodynamic characteristics are the most important. This paper describes a computational framework to study and characterize the hemodynamic environment of cerebral aneurysms in order to relate it to clinical events, such as growth or rupture. In particular, a number of hemodynamic quantities are proposed to describe the most salient features of these hemodynamic environments. Application to a patient population indicates that ruptured aneurysms tend to have concentrated inflows, concentrated wall shear stress distributions, high maximal wall shear stress, and smaller viscous dissipation ratios than unruptured aneurysms. Furthermore, these statistical associations are largely unaffected by the choice of physiologic flow conditions. This confirms the notion that hemodynamic information derived from image-based computational models can be used to assess aneurysm rupture risk, to test hypotheses about the mechanisms responsible for aneurysm formation, progression, and rupture, and to answer specific clinical questions. Copyright © 2010 John Wiley & Sons, Ltd.

Received 6 August 2010; Revised 14 October 2010; Accepted 15 October 2010

KEY WORDS: cerebral aneurysms; hemodynamics; rupture risk; patient-specific modeling

INTRODUCTION

Assessing the risk of rupture of intracranial aneurysms is important for clinicians because the natural rupture risk can be exceeded by the small but significant risk carried by current treatments [1–3]. To date, risk assessment is mainly based on aneurysm size. However, it is known that small aneurysms do rupture, and therefore a more precise risk assessment is highly desirable. Improving current aneurysm risk assessment and evaluation requires knowledge of the underlying mechanisms governing the natural evolution of cerebral aneurysms. Although these mechanisms are poorly understood, hemodynamics is thought to play a fundamental role [4–7]. Thus, numerous investigators have used image-based computational fluid dynamics (CFD) models to extract patient-specific

*Correspondence to: Juan R. Cebal, Center for Computational Fluid Dynamics, Department of Computational and Data Sciences, George Mason University, 4400 University Drive, MSN 6A2 Fairfax, VA 22030, U.S.A.

[†]E-mail: jcebral@gmu.edu

hemodynamics information [8–10]. However, there is no consensus on which variables or hemodynamic characteristics are the most important. This paper describes a computational framework to study and characterize both qualitatively and quantitatively the hemodynamic environment of cerebral aneurysms in order to relate it to clinical events, such as growth or rupture. In particular, a number of hemodynamic quantities are proposed to describe the most salient features of these hemodynamic environments and further our understanding of the mechanisms of aneurysm progression and rupture.

METHODOLOGY

Clinical and imaging data

Anatomical images of cerebral aneurysms and the connected blood vessels are obtained using 3D rotational angiography (3DRA). These images are acquired during conventional transfemoral catheterization of the cerebral blood vessels. Rotational angiograms are obtained during a 6-s contrast injection for a total of 24 cc of contrast agent and imaging at 15 frames per second over 8 s for acquisition of 120 projection images on a Philips Integris biplane unit (Philips Medical Systems, Best, the Netherlands). The projection images are reconstructed into 3D voxel data using standard proprietary software (Philips XtraVision).

The patients' medical and radiological records are reviewed and evaluated for evidence of aneurysmal intracranial hemorrhage. In patients with multiple aneurysms, the clinical and radiological information are considered and a judgment of the most likely source of hemorrhage is made. The other co-incident aneurysms are classified as unruptured. Cases with evidence of vasospasm, or incomplete or inconclusive clinical information as well as dissecting aneurysms are excluded from the study.

Vascular modeling

Patient-specific vascular models are constructed from the 3DRA images using seeded region growing segmentation to recover the arterial network topology followed by isosurface deformable models to recover the vascular geometry [11, 12]. The models are then smoothed using a non-shrinking algorithm [13] and arterial branches are truncated perpendicularly to their axes. During the vascular model construction process, the entire proximal portion of the parent artery visible in the 3D image is included in the model to ensure proper representation of secondary or swirling flows at the aneurysm location [14]. The geometrical models are then used to generate volumetric computational grids composed of tetrahedral elements using an advancing front method [12, 15]. These meshes are generated with a minimum uniform resolution of 0.01–0.02 cm. The mesh resolution is locally increased using source functions along arterial branches in order to ensure a minimum of 10–20 grid points in all vessel diameters. Typical meshes contain between 1 million and 5 million elements.

Domain subdivision

Once the volumetric grid has been generated, the computational domain is partitioned into different geographic regions. This process consists of the following steps: (a) interactive delineation of the aneurysm neck, (b) triangulation of the aneurysm orifice, (c) partition of the computational domain into aneurysm and vessel regions, and (d) further subdivision of aneurysm and vessel regions into subregions. During the interactive neck delineation, the user clicks on grid points along the aneurysm neck. When the user selects a new point, all points along the shortest path on the surface (geodesic line) from the last selected point are automatically selected. Thus, the line loop defining the aneurysm neck is delineated with a few clicks along the neck. Then, the aneurysm orifice defined by this neck line is triangulated. This neck surface is then used to split the surface and volume grids into two regions corresponding to the aneurysm and the connected arteries. This is done by first identifying all edges of the surface and volume grids

that are cut by the triangles of the neck surface. Then, a region growing algorithm is used to label all grid points on each side of the neck surface. In cases with multiple aneurysms or arterial branches emanating from the aneurysm sac, a second ‘neck’ surface is created and used to restrict the region growing algorithm. Subsequently, signed geodesic distances to the neck maps are computed on the surface and volume grids. Distances on the vessel side are assigned a negative sign and distances on the aneurysm side are assigned a positive sign. These maps are then used to subdivide the vessel and aneurysm regions into the following subregions: (1) near vessel—negative distance to the neck less than 1 cm, (2) far vessel—negative distance to the neck larger than 1 cm, (3) aneurysm neck—positive distance to the neck less than 10% of maximum positive distance, (4) aneurysm body—positive distance to the neck less than 60% of the maximum positive distance, and (5) aneurysm dome—positive distance to the neck larger than 60% of the maximum positive distance. In case of fusiform aneurysms, two ‘neck’ contours are defined. This allows us to separate the aneurysmal segment from the parent artery. However in these cases, it is not possible to further subdivide the aneurysm into neck, body, or dome regions. The procedure for geographic labeling of the vascular model is illustrated in Figure 1.

We denote Ω as the computational domain, which is partitioned into an aneurysm volume (Ω_a) and a vessel volume (Ω_v): $\Omega = \Omega_a + \Omega_v$. Similarly, the domain surface Γ , which is defined as the boundary of the computational domain ($\Gamma_0 = \partial\Omega$), is partitioned into an aneurysm surface (Γ_a) and a vessel surface (Γ_v): $\Gamma = \Gamma_a + \Gamma_v$. The surface of the aneurysm orifice Γ_o divides the aneurysm and vessel regions and its boundary coincides with the neck contour delineated by the user (N): $\Gamma_o = \partial N$.

Hemodynamics modeling

Blood flows are mathematically modeled using the unsteady 3D Navier–Stokes equations for an incompressible Newtonian fluid with density $\rho = 1.0 \text{ g/cm}^3$ and viscosity $\mu = 0.04 \text{ P}$. The governing equations are advanced in time using a fully implicit scheme that recasts the original equations as a steady-state problem in pseudo time (ϑ) at each time step (n):

$$u^{\xi, \vartheta} + u^{\xi} \cdot \nabla u^{\xi} + \nabla p^{\xi} = \nabla \eta \nabla u^{\xi} - \frac{u^{\xi} - u^n}{\xi \Delta t} \quad (1)$$

$$\nabla \cdot u^{\theta} = 0 \quad (2)$$

where u is the velocity, p the pressure, η the kinematic viscosity, u^n denotes the velocity at the previous time step, and $u^{\xi} = (1 - \xi)u^n + \xi u^{n+1}$. The parameter ξ selects the numerical scheme as: first-order implicit Euler scheme ($\xi = 1$), first-order explicit Euler scheme ($\xi = 0$), and second-order Crank–Nicholson scheme ($\xi = 1/2$). These equations are solved using a pressure–projection method where the spatial discretization is carried out using an edge-based upwind finite element method [15]. The discretized momentum equation is solved using a Generalized Minimal Residuals (GMRES) method and the discretized pressure Poisson equation is solved using a deflated preconditioned conjugate gradients method [16]. The latter method has been shown to significantly reduce the computation time, especially for elongated or tubular domains.

Typically, patient-specific blood flow data is not collected as part of the routine clinical examinations, and thus this information is not commonly available. Therefore, typical flow waveforms obtained from *in vivo* measurements of blood flows in normal subjects using phase-contrast magnetic resonance are used to prescribe boundary conditions [17–19]. The waveforms measured in the cerebral arteries of normal volunteers are scaled with the area of the inlet boundary in order to achieve a mean wall shear stress (WSS) of 15 dyne/cm^2 at the inlet [19]. Fully developed velocity profiles are mapped to the inlet boundary using the Womersley solution [20]. Previous studies suggest that this is a reasonable approach provided that a long enough portion of the proximal parent artery is included in the vascular model [21]. Outflow boundary conditions are selected to avoid producing unphysiologic pressure drops along the different arterial branches. Traction-free boundary conditions are prescribed at the large model outlets. However, if the model contains small arterial branches, the flow rate in those branches is estimated in order to avoid

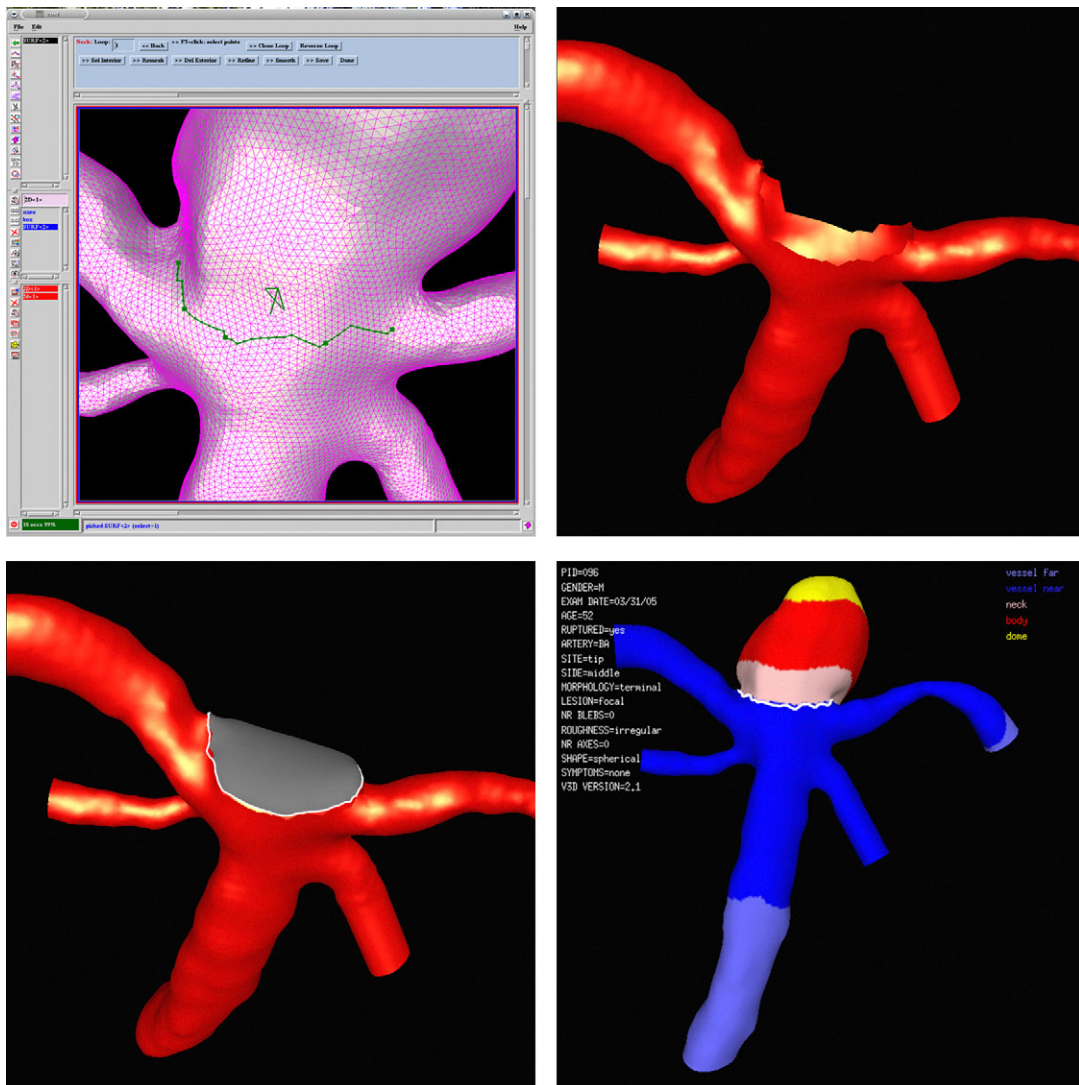


Figure 1. Geographic subdivision of the vascular model: interactive delineation of the aneurysm neck (top left), removal of aneurysm sac (top right), triangulation of neck surface (bottom left), and subdivision of aneurysm and vessel into subregions using the neck surface (bottom right).

a large change in the WSS from the parent artery and imposed as outflow boundary conditions. No-slip boundary conditions ($u = 0$) are imposed at the vessel walls. As patient-specific flows are not known, each model is run under a range of physiologic flow conditions in order to assess the variability of the resulting hemodynamic variables. Specifically, each model is run under two pulsatile flow waveforms corresponding to heart rates of 60 and 100 bpm [22], and three steady flow conditions corresponding to an inlet WSS of 10 (low), 15 (medium), and 20 dyne/cm² (high), respectively. The pulsatile simulations are carried out for two cardiac cycles using 100 time steps per cycle. It has been previously verified that results from the second and third cycles coincide; therefore in these cases results are presented for the second cycle.

Blood flow post-processing

In order to investigate the role of hemodynamics in the mechanisms of aneurysm initiation, progression, and rupture, the unsteady flow velocity field is post-process to define different derived quantities. These derived fields can be subdivided into (a) volumetric fields, (b) surface fields, and

(c) fields defined at the aneurysm orifice surface. These fields are defined as described in what follows.

Volumetric fields

Derived fields defined over the domain volume include: kinetic energy (k), strain rate ($\dot{\gamma}$), viscous dissipation (Φ), and vorticity (ω), defined as

$$k = \frac{1}{2} \rho u^2 \tag{3}$$

$$\dot{\gamma} = 2 \sqrt{e_{ij} e_{ij}} \tag{4}$$

$$\Phi = \frac{1}{2} \eta \dot{\gamma}^2 \tag{5}$$

$$\omega = \nabla \times u \tag{6}$$

where the strain rate tensor (e_{ij}) is given by

$$e_{ij} = \frac{1}{2} \left(\frac{\partial u_i}{\partial x_j} + \frac{\partial u_j}{\partial x_i} \right) \tag{7}$$

These fields are numerically computed from the velocity field using a Galerkin finite element approximation in the volumetric domain Ω .

Surface fields

Surface fields derived over the domain surface include: WSS (τ), wall shear stress gradient (WSSG), and oscillatory shear index (OSI). The WSS field is calculated as the derivative of the tangential velocity (u_t) in the normal direction (n) at the vessel surface:

$$\tau = \frac{\partial u_t}{\partial n} \tag{8}$$

This field is computed from the velocity field using a parabolic recovery of boundary gradients method. It has been shown that this second-order method produces results similar to those obtained with a boundary layer mesh with three grid points in the boundary layer [23]. The OSI is computed as

$$OSI = \frac{1}{2} \left(1 - \frac{|\langle \tau \rangle|}{\langle |\tau| \rangle} \right) \tag{9}$$

where

$$|\langle \tau \rangle| = \frac{1}{T} \left| \int_0^T \tau dt \right| \quad \text{and} \quad \langle |\tau| \rangle = \frac{1}{T} \int_0^T |\tau| dt \tag{10}$$

with the integral taken over the cardiac cycle period (T). The WSSG is computed by taking the derivatives of the WSS magnitude on the vessel surface in two directions given by the flow direction (α) and normal to it (β):

$$WSSG = \sqrt{\left(\frac{\partial \tau}{\partial \alpha} \right)^2 + \left(\frac{\partial \tau}{\partial \beta} \right)^2} \tag{11}$$

$$\frac{\partial \tau}{\partial \alpha} = \nabla \tau \cdot \alpha, \quad \frac{\partial \tau}{\partial \beta} = \nabla \tau \cdot \beta, \quad \alpha = \frac{\tau}{|\tau|}, \quad \beta = n \times \alpha$$

where n is the normal to the surface and the gradient operator ∇ denotes partial derivatives in the coordinate directions. These derivatives are calculated using a Galerkin finite element approximation over the surface mesh Γ .

Orifice fields

Finally, the velocity field is interpolated to the orifice surface Γ_o . This is done by first identifying all the edges of the volume grid that are cut by triangles of the surface defining the neck surface. The algorithm uses a bin data structure to store all the edges of the volume grid. Then it loops over all the neck surface triangles and identifies from the bin structure the edges crossing the bounding box of each triangle. These edges are tested to check whether they cut the triangle plane and if so, if the intersection point lies inside the triangle, in which case the edge is marked as cut. Once the cut edges have been found, linear interpolation is used to compute the field values at the intersection points. A triangular connectivity is then generated connecting the intersection points into an interpolated neck surface mesh. Using this connectivity, the surface normal at each point on the orifice surface is computed and used to find the velocity components along the orifice surface (u_s) and perpendicular to it (u_p).

Blood flow visualization

In order to visually inspect the results of the CFD simulations and qualitatively characterize the aneurysmal hemodynamics, a number of pre-defined visualizations are automatically created. First, streamlines color-coded with the velocity magnitude are used to visualize the instantaneous flow structures. A number of streamline origins are automatically created and saved by randomly selecting uniformly distributed points in the aneurysm and near vessel regions. For each of these points a streamline is propagated in the forward (positive) and backward (negative) velocity directions. This ensures proper visualization of the flow structures in the aneurysm and parent vessel. Second, isovelocity surfaces are used to visualize the flow streams in the parent artery and the aneurysm at each time instant. Third, a plane that attempts to cut the aneurysm neck through the inflow stream is automatically calculated. This plane passes through the centroid of the aneurysm neck surface. Its normal is computed as the cross product of the aneurysm neck normal at the centroid with the vector that goes from the centroid to the point on the neck surface that has the maximum inflow velocity. Visualizations of the inflow stream and aneurysm flow structure are then created by plotting the velocity magnitude interpolated to this cutting plane. The velocity field is further visualized by plotting velocity vectors color-coded with the velocity magnitude over the entire computational domain. Then, the distributions of WSS, WSSG, and OSI are visualized using surface shading plots color-coded with the magnitude of these variables. Additionally, the aneurysm geometry and its subdivision into different regions are visualized by plotting the aneurysm surface triangulation color-coded with the region labels and a line delineating the neck surface boundary. Examples of these visualizations are presented in Figure 2.

All these operations are created in two modes of operations: (a) interactive or visual exploration mode and (b) passive or visual inspection mode. In the first mode, the operator can interactively rotate, translate, and zoom the scene while the graphical objects (e.g. isovelocity surfaces) are animated through the cardiac cycle. In the second mode, an animation is automatically created and saved to a file. As the user cannot interact with the scene in this mode, the most appropriate aneurysm view is set as follows. The viewpoint is translated to the centroid of the aneurysm region, and the zooming factor is computed from the ratio of the aneurysm bounding box to the bounding box of the entire computational domain in order to fit the aneurysm and a portion of the parent artery into the screen. Then, the model is rotated around an axis in the vertical direction passing through the aneurysm centroid. The rotation speed is set such that four cardiac cycles are displayed for one complete rotation. In this way it is possible to observe the pulsating flow fields from all view points around the aneurysm. All these visualizations are created with in-house software that uses a script system to automate the visualizations and that operates in off-screen mode for non-interactive visualizations [24].

Qualitative hemodynamics characterization

The aneurysmal hemodynamic environment is qualitatively characterized by visual inspection of the blood flow visualizations according to the following properties [25]: (1) *flow complexity*: simple

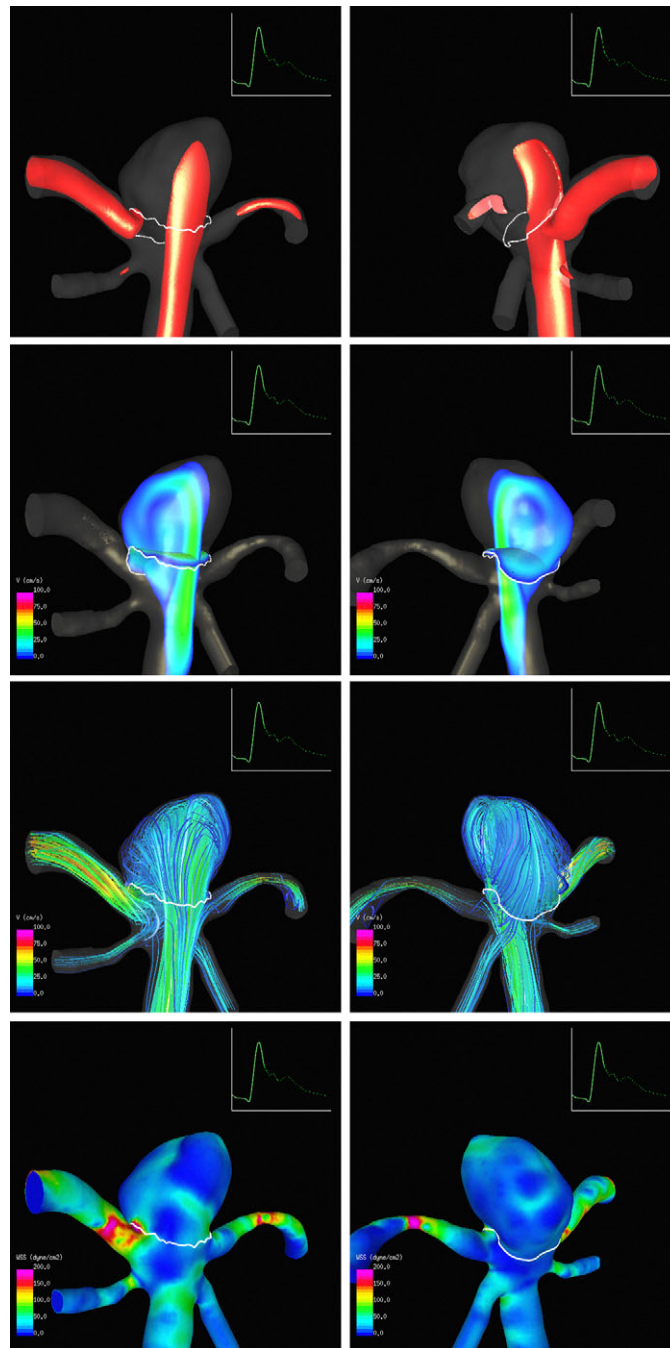


Figure 2. Examples of flow visualizations created automatically from two viewpoints (top and bottom rows) and one instant of time. From left to right the flows are visualized using isovelocity surfaces, velocity magnitudes on a cut plane and the neck surface, streamlines colored with the velocity magnitude, and the distribution of wall shear stress.

flow patterns consisting on a single recirculation zone or vortex structure within the aneurysm, or complex flow patterns exhibiting flow divisions or separations within the aneurysm sac and containing more than one recirculation zone or vortex structure; (2) *flow stability*: stable flow patterns that persist (do not move or change) during the cardiac cycle, or unstable flow patterns where the flow divisions and/or vortex structures move or are created or destroyed during the

cardiac cycle; (3) *inflow concentration*: concentrated inflow streams or jets that penetrate relatively deep into the aneurysm sac and are thin or narrow in the main flow direction, or diffuse inflow streams that are thick compared to the aneurysm neck and flow jets that disperse quickly once they penetrate into the aneurysm sac; and (4) *flow impingement*: the flow impingement zone is the region of the aneurysm where the inflow stream is seen to impact the aneurysm wall and change its direction and/or disperse. This region is classified as small (large) if its area is small (large) compared to the area of the aneurysm (less than 50% or more than 50%).

Quantitative hemodynamics data reduction

Motivated by previous studies that have shown associations between the qualitative hemodynamic characteristics described above and aneurysm rupture [25, 26], quantitative variables that attempt to capture the salient features of these qualitative characteristics were defined. Using the geographic subdivision of the computational domain described earlier, the following quantities are defined using hemodynamic variables defined over the volume, surface, or orifice regions:

Kinetic energy ratio (KER) measures the average kinetic energy in the aneurysm relative to that of the parent artery

$$KER = \frac{k_a}{k_v} = \frac{\int_{\Omega_a} \frac{1}{2} \rho u^2 d\Omega / \int_{\Omega_a} d\Omega}{\int_{\Omega_v} \frac{1}{2} \rho u^2 d\Omega / \int_{\Omega_v} d\Omega} \quad (12)$$

where k_a and k_v represent the average kinetic energy computed over the aneurysm (Ω_a) and near vessel regions (Ω_v), respectively.

Viscous dissipation ratio (VDR) measures the average amount of viscous dissipation of mechanical energy in the aneurysm relative to that in the parent artery

$$VDR = \frac{\Phi_a}{\Phi_v} = \frac{\int_{\Omega_a} \frac{1}{2} \eta \dot{\gamma}^2 d\Omega / \int_{\Omega_a} d\Omega}{\int_{\Omega_v} \frac{1}{2} \eta \dot{\gamma}^2 d\Omega / \int_{\Omega_v} d\Omega} \quad (13)$$

where Φ_a and Φ_v represent the average mechanical dissipation in the aneurysm and near vessel regions, respectively.

Maximal wall shear stress (MWSS) measures the maximum WSS value over the aneurysm region

$$MWSS = \max_{\Gamma_a}(\tau) \quad (14)$$

Denoting τ_v and σ_v as the mean and standard deviation of the WSS magnitude computed over the near vessel region, aneurysm regions of high (Γ_h) and low (Γ_l) WSS are defined as regions where the WSS is higher or lower than the mean WSS in the parent artery by one standard deviation

$$\begin{aligned} \Gamma_h &= \{x \in \Gamma_a / \tau(x) > \tau_v + \sigma_v\} \\ \Gamma_l &= \{x \in \Gamma_a / \tau(x) < \tau_v - \sigma_v\} \end{aligned} \quad (15)$$

The areas of these two regions are denoted by A_h and A_l , respectively. In addition to MWSS, the following surface variables are defined.

Low shear area (LSA) measures the percent of the aneurysm area that is subject to a ‘low’ WSS, i.e. one standard deviation below the mean WSS in the parent artery:

$$LSA = A_l / A_a \quad (16)$$

where A_a is the area of the aneurysm sac. This variable is 0 if there is no region with WSS below one standard deviation of the mean WSS in the parent artery, and will tend to 1 if the entire aneurysm is subject to ‘low’ WSS.

Shear concentration index (SCI) measures the degree of concentration of the WSS distribution

$$SCI = \frac{F_h/F_a}{A_h/A_a} \quad (17)$$

where F_h and F_a represent the total viscous shear force computed over the region of WSS (Γ_h) and the entire aneurysm (Γ_a), respectively

$$F_h = \int_{\Gamma_h} |\tau| d\Gamma, \quad F_a = \int_{\Gamma_a} |\tau| d\Gamma \quad (18)$$

This index becomes 0 if no part of the aneurysm is under ‘high’ WSS (higher than one standard deviation above the mean WSS in the parent artery) and becomes large when the WSS distribution has a peak with high WSS concentrated on a small region of the aneurysm.

Low shear index (LSI) measures the relative amount of the total shear force that is applied in regions of ‘low’ WSS

$$LSI = \frac{F_l A_l}{F_a A_a} \quad (19)$$

where F_l is the total viscous shear force applied in the region of ‘low’ WSS

$$F_l = \int_{\Gamma_l} |\tau| d\Gamma \quad (20)$$

The LSI varies from 0 when no frictional shear force is applied in regions of low WSS to 1 when the total frictional shear force is applied in regions of low WSS.

Defining Γ_i the inflow region of the aneurism orifice, i.e. with positive normal velocity

$$\Gamma_i = \{x \in \Gamma_0 / u_n > 0\} \quad (21)$$

the areas of the inflow and entire aneurysm orifice are denoted as A_i and A_o , respectively.

Inflow concentration index (ICI) measures the degree of concentration of the blood stream flowing from the parent artery into the aneurysm

$$ICI = \frac{Q_i/Q_v}{A_i/A_o} \quad (22)$$

where Q_v is the flow rate in the parent artery and Q_i is the flow rate entering the aneurysm

$$Q_i = \int_{\Gamma_i} u_p d\Gamma \quad (23)$$

This index takes a value of 0 if no flow enters the aneurysm and grows larger as the flow rate increases and is concentrated over a small region of the aneurysm orifice.

Data organization and archival

All the clinical, imaging, and simulation data are organized using a consistent naming and directory structure. The clinical information consists of a text file listing the patient’s age, gender, symptoms, aneurysm location, history of SAH, etc. The imaging data contains the original 3D images used to construct the computational models. The simulation data consists of the computational grid, the definition of the aneurysm neck, the labeling of the different regions, the flow boundary conditions, and the results of the different simulations. This data is then augmented by the data generated during post-processing, data reduction, and visualization and characterization steps. The logical and consistent organization of the data allows us to create simple scripts to automate several operations, such as constructing tables, performing statistics, and creating bar charts of scatter plots of the different hemodynamic and geometrical variables. This organization and set of scripts are very flexible compared with a traditional database organization because it allows us to easily add,

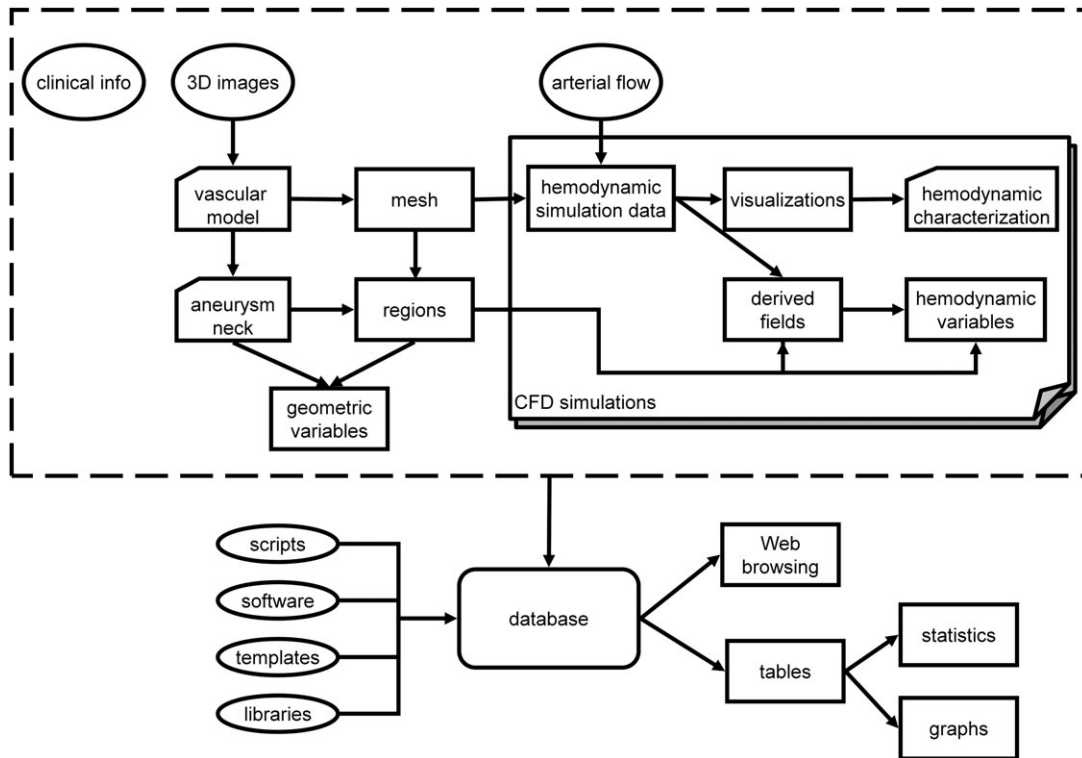


Figure 3. Schematics of the data organization and relationship within the computational framework for the analysis of cerebral aneurysms.

delete, or modify variables and relationships, and recreate tables and plots quickly. Furthermore, if desired, it is easy to create tables that can then be imported into a relational database, for instance for performing complex queries or other operations. Additionally, a set of scripts are used to automatically create a web page for browsing the database. This web page presents the clinical, anatomical, and hemodynamic data of each aneurysm using the pre-computed non-interactive visualizations. This is very useful to allow physicians to easily inspect and analyze the data simply with a web browser.

The organization of the database is schematically shown in Figure 3. Rectangular boxes represent data generated automatically. Boxes with a truncated corner represent data generated with procedures that require some level of user interaction. Elliptical boxes represent clinical, imaging, physiologic, or other basic data or information. The dotted box represents the data corresponding to a single aneurysm, which in turn contains a number of CFD simulations.

Data analysis

For each aneurysm, the values of all the variables defined above are computed at each instant of time during the cardiac cycle and their minimum, maximum, and average values over the cardiac cycle calculated. Then, different aneurysm groups are defined, including ruptured and unruptured aneurysms, aneurysms with complex or simple flows, aneurysms with stable or unstable flows, aneurysms with concentrated or diffuse inflows, and aneurysms with small or large flow impingement regions. The average values of these variables over the different aneurysm groups are then computed and statistically compared using Student's *t*-test. The differences in the mean values are considered statistically significant if the two-tailed *p*-values were less than 0.05 (95% confidence).

Finally, the ratios of the mean values of the hemodynamic variables over the different aneurysm groups are computed and their variability with flow conditions and manual neck delineation are determined.

RESULTS

A total of 210 cerebral aneurysms have been modeled, characterized, organized into a database system, and analyzed using the methodology described earlier. Quantitative hemodynamic variables extracted from the simulations were compared to the previous history of aneurysm rupture and to qualitative hemodynamic characteristics assigned by visual inspection. For completeness, the aneurysm size and aspect ratio are also computed. The aneurysm size is defined as the maximum Euclidean distance between any two points belonging to the aneurysm region. The aspect ratio is defined as the aneurysm depth divided by the aneurysm neck size. The depth is computed as the maximum length of the minimal path in the aneurysm volume connecting any point on the aneurysm sac and the aneurysm orifice. The aneurysm neck size is the maximum Euclidean distance between any two points of the aneurysm orifice.

Ruptured vs unruptured aneurysms

Table I lists the average values of geometric and hemodynamic variables computed over the ruptured and unruptured aneurysm groups. The two-tailed *p*-values corresponding to the *t*-test comparison of the mean values over each group are also listed. The ratios of the mean values of ruptured aneurysms over unruptured aneurysms are also shown graphically in Figure 4. The stars over the bars of this figure indicate a statistically significant difference between the mean values of ruptured and unruptured aneurysms. The results presented in Table I and Figure 4 indicate that rupture aneurysms tend to have larger sizes, larger aspect ratios, larger MWSS, larger inflow concentrations, larger shear concentrations, and lower viscous dissipation than unruptured aneurysms. They also tend to have larger KERs but this variable did not reach statistical significance. Additionally the areas under low WSS and the LSIs of ruptured and unruptured aneurysms were not statistically different.

Variability with neck delineation and flow conditions

In order to study the variability of geometric and hemodynamic variables with respect to the manual delineation of the aneurysm neck, the neck contour was traced twice in a subset of 10 aneurysms, and the relative change in the variables was calculated. Table II lists the relative change in the ratio of mean geometric and hemodynamic variables of ruptured to unruptured aneurysms (Δ_N). The relative change in the ratio of geometric variables is well within 10%. On the other hand, the relative change in the ratio of hemodynamic variables exhibits a larger variability, reaching a maximum of approximately 30%.

Similarly, the variability of the *difference* in hemodynamic variables between ruptured and unruptured aneurysms with respect to the physiologic flow conditions was analyzed. Table II shows the maximum relative change in the ratio of hemodynamic variables of ruptured to unruptured aneurysms obtained with the different flow conditions described before (Δ_Q). It can be seen that although the values of hemodynamic variables change with the flow conditions, their proportion

Table I. Values of geometric and hemodynamic variables averaged over the ruptured and unruptured aneurysm groups and the corresponding *t*-test *p*-values.

	Variable	Ruptured	Unruptured	<i>p</i> -value
Geometry	Size	9.38 mm	6.59 mm	<0.0001
	AR	1.42	0.966	<0.0001
Hemodynamics	MWSS	384 dyn/cm ²	277 dyn/cm ²	0.0034
	ICI	1.012	0.66	0.0035
	SCI	9.97	6.47	0.0154
	VDR	0.36	0.951	0.0123
	KER	0.232	0.176	0.2226
	LSA	60%	56%	0.3716
	LSI	0.26	0.25	0.6630

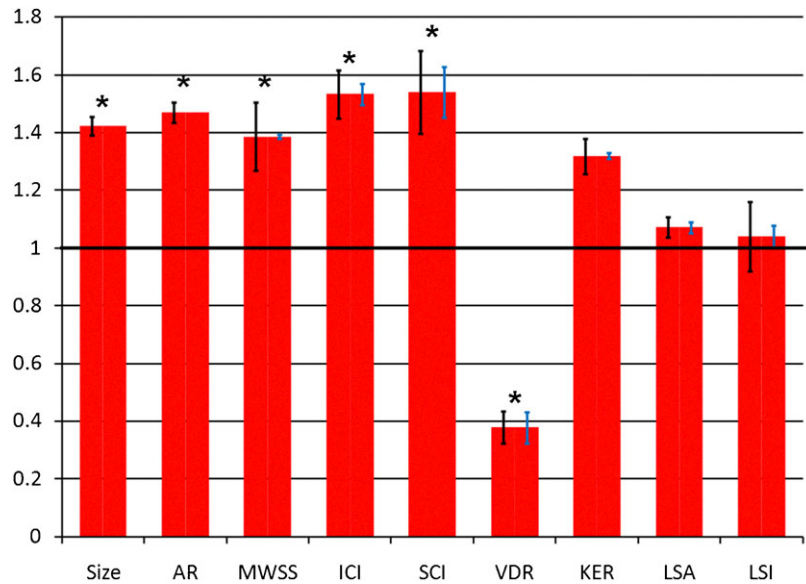


Figure 4. Ratio between variables averaged over ruptured aneurysms and variables averaged over unruptured aneurysms. Error bars indicate variability of this ratio with respect to delineation of the aneurysm neck (left bars) and to flow conditions (right bars). Stars indicate statistically significant differences between the mean values.

Table II. Variability of the ratio of mean quantities of ruptured to unruptured aneurysm groups with respect to the manual delineation of the aneurysm neck (Δ_N) and flow conditions (Δ_Q).

	Variable	Δ_N (%)	Δ_Q (%)
Geometry	Size	6.3	—
	AR	7.2	—
Hemodynamics	MWSS	23.8	7.1
	ICI	16.6	1.6
	SCI	28.7	17.5
	VDR	11.2	10.7
	KER	12.3	2.0
	LSA	7	3.7
	LSI	24.1	7.5

over the ruptured and unruptured groups remains within a maximum of up to 17% relative difference.

The two sets of error bars included in Figure 4 represent the variability of the ratios of geometric and hemodynamic variables of ruptured to unruptured aneurysms with respect to the neck tracing (left bars) and the flow conditions (right bars). The statistical difference of mean values between ruptured and unruptured aneurysms, indicated by the stars in Figure 4, was not affected by either the new neck delineation or the flow conditions.

Qualitative characteristics and quantitative measures

The relationship between the qualitative hemodynamic categories previously studied and quantitative hemodynamics and geometric measures are presented in Tables III and IV, respectively. These tables list, for each dichotomous flow category (flow complexity, flow stability, inflow concentration, impingement size) the average of each quantitative variable over the two possible groups of aneurysms and the corresponding *t*-test *p*-value. The ‘yes’ rows of these tables represent the groups of aneurysms that have complex flows, unstable flows, concentrated inflows, and small impingement regions. In contrast, the ‘no’ rows represent the groups of aneurysms that have

Table III. Hemodynamic variables averaged over the different categories used for qualitative hemodynamic characterization of aneurysms, and corresponding *p*-values of Student's *t*-test of the statistical difference between the mean values of each category.

Category		Variable						
		MWSS	ICI	SCI	VDR	KER	LSA	LSI
Complex flow	Yes	354	1.003	9.87	0.299	0.202	62%	0.265
	No	258	0.440	4.31	1.456	0.199	51%	0.244
	<i>p</i>	0.0099	<0.0001	0.0001	<0.0001	0.8260	0.0224	0.5335
Unstable flow	Yes	296	1.011	10.4	0.208	0.169	67%	0.316
	No	357	0.449	3.55	1.562	0.246	41%	0.158
	<i>p</i>	0.1048	<0.0001	<0.0001	<0.0001	0.0907	<0.0001	<0.0001
Concentrated inflow	Yes	386	1.114	10.39	0.264	0.194	65%	0.294
	No	262	0.529	5.67	1.107	0.201	52%	0.224
	<i>p</i>	0.0005	<0.0001	0.0007	0.0002	0.8818	0.0048	0.0301
Small impingement	Yes	324	0.869	9.99	0.260	0.156	67%	0.309
	No	311	0.691	4.51	1.431	0.264	42%	0.174
	<i>p</i>	0.7235	0.1418	0.0001	<0.0001	0.0185	<0.0001	<0.0001

Table IV. Geometric variables averaged over the different categories used for qualitative hemodynamic characterization of aneurysms, and corresponding *p*-values of Student's *t*-test of the statistical difference between the mean values of each category.

Category		Variable	
		Size	AR
Complex flow	Yes	9.41	1.421
	No	4.67	0.688
	<i>p</i>	<0.0001	<0.0001
Unstable flow	Yes	9.51	1.42
	No	4.68	0.70
	<i>p</i>	<0.0001	<0.0001
Concentrated inflow	Yes	10.46	1.54
	No	5.31	0.80
	<i>p</i>	<0.0001	<0.0001
Small impingement	Yes	8.72	1.39
	No	6.08	0.76
	<i>p</i>	<0.0001	<0.0001

simple flows, stable flows, diffuse inflows, and large impingement regions. These results are also presented graphically in Figures 5 and 6. These figures show, for each flow category, the ratio of the mean value of each quantity over the 'yes' group to the 'no' group. Stars over the bars indicate statistically significant differences in the mean values of the 'yes' and 'no' groups.

These results suggest that aneurysms with complex flows are more likely associated to higher MWSS, higher ICIs, higher SCIs, lower VDRs, and higher areas of low WSS than those with simple flows. However, complex and simple flows have equal mean KERs and LSIs.

Aneurysms with unstable flows are more likely to have larger ICIs, larger SCIs, lower VDRs, larger areas under low WSS, and higher LSIs than aneurysms with stable flows. They also have lower KERs but this relationship is only within the 90% confidence interval (indicated with a plus sign in Figure 5). The mean MWSS of stable and unstable flows are not statistically different.

Aneurysms with concentrated inflow jets have larger MWSS, larger ICIs, larger SCIs, smaller VDRs, larger areas under low WSS, and larger LSIs than aneurysms with diffuse inflow jets. KERs between these groups are not statistically different.

Aneurysms classified as having small impingement regions tend to have larger shear concentration indices, smaller VDRs, smaller KERs, larger areas under low WSS, and larger LSIs than those with large impingement regions. However, the MWSS and ICIs of these two groups were not statistically different.

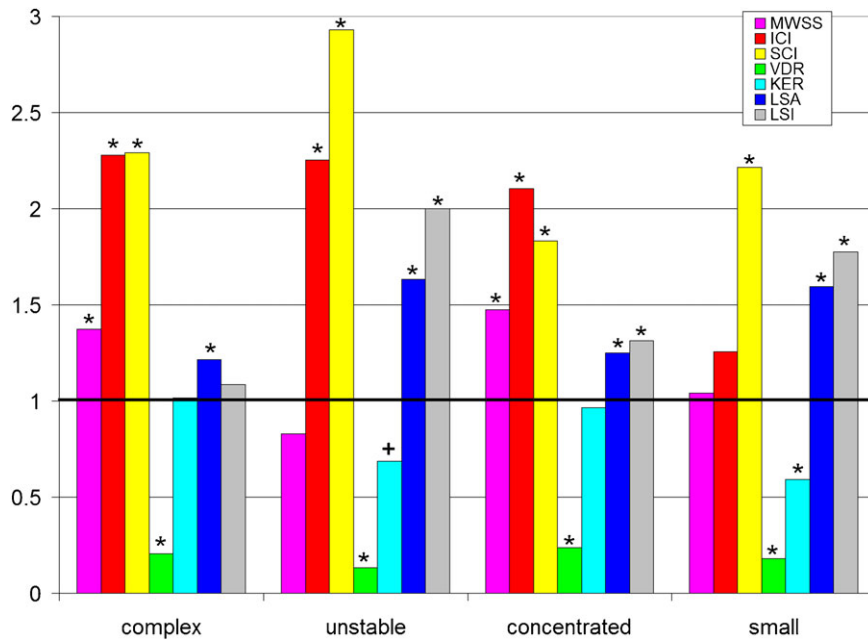


Figure 5. Ratio of hemodynamic variables averaged over each flow category. Stars indicate statistically significant differences between the mean values of the corresponding variables.

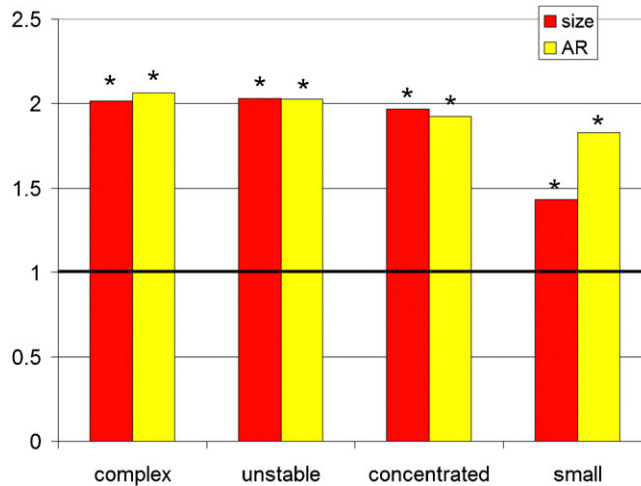


Figure 6. Ratio of geometric variables averaged over each flow category. Stars indicate statistically significant differences between the mean values of the corresponding variables.

Finally, complex flows, unstable flows, concentrated inflows, and small impingement regions were all associated with larger aneurysm sizes and aspect ratios.

DISCUSSION

This paper described a methodology to analyze the patient-specific hemodynamic environment in cerebral aneurysms in order to relate qualitative hemodynamic characteristics and quantitative

measures to clinical events such as aneurysm rupture in order to shed light on the mechanisms that govern the natural history of intracranial aneurysms. The methodology was illustrated by studying statistically the relationship between hemodynamic quantities and the previous history of aneurysm rupture [27], in which it was shown that ruptured aneurysms tend to have concentrated inflows and shear stress distributions, high MWSS values, lower viscous dissipation than their parent arteries, and marginally larger kinetic energies than their parent arteries. In contrast, ruptured and unruptured aneurysms did not have statistically different areas under low WSS of LSIs. Statistically significant hemodynamic differences between ruptured and unruptured aneurysms first reported by Cebra *et al.* [26] are confirmed by the current results. Additionally, it was shown that these relationships are not significantly affected by the manual delineation of the aneurysm neck contour or by the choice of physiologic flow conditions (including the use of steady flows). The development of objective automatic algorithms for aneurysm neck delineation [28, 29] could further improve the reproducibility and robustness of the hemodynamic data reduction and thus reduce the variability of quantitative measures.

It is generally accepted that the pathophysiology of cerebral aneurysms is a complex multifactorial problem. The current theories implicate genetic factors, peri-aneurysmal environment, and vascular biology in combination with the hemodynamic environment as determinant of which aneurysms will enlarge and ultimately rupture [5]. Aneurysm enlargement in particular is thought to be the result of the interaction between hemodynamic loads and mechano-biological responses of the cellular elements of the wall that result in wall weakening followed by passive yield to pressure. This process can stabilize or continue until wall stress exceeds wall strength and aneurysm ruptures. Although hemodynamics is widely considered as of fundamental importance in this process, there is no consensus on which variables or hemodynamic characteristics are most important. Great controversy exists whether regions of low or high flow are the most critical in promoting the events responsible for growth and rupture. Low flow theories suggest that the presence of a low flow or stagnant environment could potentially lead to changes in the arterial wall that would weaken its structural integrity through mechanisms related to thrombus formation adjacent to the aneurysm wall and subsequent wall inflammation [30–32]. In contrast, high flow theories are based on the fact that at high levels of WSS the endothelium releases nitrous oxide that leads to remodeling of the arterial wall in a system which seeks to maintain the WSS within acceptable range [33–35]. At excessive levels of WSS, the endothelium becomes dysfunctional and can be destroyed [36]. Previous studies identified qualitative characteristics of cerebral aneurysm's hemodynamic environment that were related to aneurysm rupture [25, 26]. The current work attempts to link these qualitative characteristics to quantitative hemodynamic measures and then in turn connect these quantities to aneurysm rupture. Although the current study seems to favor theories of aneurysm progression and rupture based on high flow effects, the dependence or independence of high and low flow measures defined here need further analysis and will be part of future research.

The computational modeling approach has several limitations that should be considered when interpreting the results. First, blood is approximated as a Newtonian fluid. Previous studies have shown that non-Newtonian effects are small in large arteries [37]. However, it has not been fully demonstrated whether these effects are important in patient-specific geometries of aneurysms. Second, vessel walls are considered rigid. Previous studies suggest that wall motion does not substantially affect the hemodynamics [38, 39]. Including wall compliance into the CFD models is challenging because it either requires measurement of the wall motion to impose moving wall boundary conditions or fluid–solid interaction simulations that need information or measurements of the material characteristics of the vascular wall and the intra-arterial pressure waveforms. Third, usually measurement of patient-specific flow conditions is not part of the clinical procedures. Therefore, typical flow waveforms derived from measurements on groups of normal subjects are used to impose boundary conditions. In an attempt to estimate the most appropriate physiologic conditions for arteries of different diameters, the flow rates are scaled with the vessel area [19]. Other approaches, such as coupling the 3D models to reduced 1D or compartment models, have been suggested [40]. In any case, the physiologic conditions do change during the day and the subject's activity, and therefore it is important to understand how these normal variations influence

the hemodynamic characteristics. The current study partially addresses this question showing that some of the statistical associations between hemodynamic characteristics and aneurysm rupture are reproducible under different flow conditions. Despite all these approximations and assumptions, the current results indicate that the methodology described can produce useful statistical associations between hemodynamic variables and clinical events such as aneurysm rupture. Further analysis of the variability of hemodynamic quantities and their association with clinical observations with respect to the different assumptions and approximations is important to identify aspects of the modeling chain that need to be improved and/or refined.

CONCLUSIONS

A computational framework for the analysis of hemodynamics of cerebral aneurysms has been described. This framework includes a computational modeling pipeline to construct patient-specific models from 3D image data, tools for automatic post-processing and visualization of the results and extraction of relevant hemodynamic quantities, a database infrastructure to organize all the clinical, imaging, and simulation data, and tools for automatically creating web pages to browse the contents of the database. A number of quantitative measures have been defined and computed over a patient population with a total of 210 cerebral aneurysms. This analysis indicates that ruptured aneurysms tend to have concentrated inflows, concentrated WSS distributions, high MWSS, and smaller VDRs than unruptured aneurysms. Additionally, ruptured aneurysms tended to be larger in size and to have larger aspect ratios than unruptured aneurysms, as expected. All these associations reached a strong statistical significance. In addition, these statistical associations are largely unaffected by the physiologic flow conditions even if steady flows are used. This confirms the notion that hemodynamic information derived from image-based CFD models can be used to assess aneurysm rupture risk, to test hypotheses about the mechanisms responsible for aneurysm formation, progression and rupture, and to answer specific clinical questions.

ACKNOWLEDGEMENTS

We thank Philips Medical Systems and the National Institutes of Health (grant # R01NS059063) for financial support.

REFERENCES

1. Kassell NF, Torner JC, Haley ECJ, Jane JA, Adams HP, Kongable GL. The international cooperative study on the timing of aneurysm surgery. Part 1: overall management results. *Journal of Neurosurgery* 1990; **73**(1):18–36.
2. Wiebers DO, Whisnant JP, Huston III J, Meissner I, Brown RDJ, Piepgras DG, Forbes GS, Thielens K, Nichols D, O’Fallon WM, Peacock J, Jaeger L, Kassell N, Kongable-Beckman GL, Torner JC. International study of unruptured intracranial aneurysms investigators. Unruptured intracranial aneurysms: natural history, clinical outcome, and risks of surgical and endovascular treatment. *Lancet* 2003; **362**(9378):103–110.
3. Tomasello F, D’Avella D, Salpietro FM, Longo M. Asymptomatic aneurysms. Literature meta-analysis and indications for treatment. *Journal of Neurosurgical Science* 1998; **42**(1):47–51.
4. Stehbens WE. Intracranial aneurysms. *Pathology of the Cerebral Blood Vessels*. CV Mosby: St Louis, Missouri, 1972; 351–470.
5. Sforza D, Putman CM, Cebra JR. Hemodynamics of cerebral aneurysms. *Annual Review of Fluid Mechanics* 2009; **41**:91–107.
6. Kayembe KNT, Sasahara M, Hazama F. Cerebral aneurysms and variations of the circle of Willis. *Stroke* 1984; **15**:846–850.
7. Nixon AM, Gunel M, Sumpio BE. The critical role of hemodynamics in the development of cerebral vascular disease. *Journal of Neurosurgery* 2009; PMID: 19943737.
8. Shojima M, Oshima M, Takagi K, Torii R, Hayakawa M, Katada K, Morita A, Kirino T. Magnitude and role of wall shear stress on cerebral aneurysm: computational fluid dynamic study of 20 middle cerebral artery aneurysms. *Stroke* 2004; **35**(11):2500–2505.
9. Steinman DA, Milner JS, Norley CJ, Lownie SP, Holdworth DW. Image-based computational simulation of flow dynamics in a giant intracranial aneurysm. *AJNR American Journal of Neuroradiology* 2003; **24**(4):559–566.

10. Jou LD, Quick CM, Young WL, Lawton MT, Higashida R, Martin A, Saloner D. Computational approach to quantifying hemodynamic forces in giant cerebral aneurysms. *AJNR American Journal of Neuroradiology* 2003; **24**(9):1804–1810.
11. Yim PJ, Boudewijn G, Vasbinder B, Ho VB, Choyke PL. Isosurfaces as deformable models for magnetic resonance angiography. *IEEE Transactions on Medical Imaging* 2003; **22**(7):875–881.
12. Cebral JR, Castro MA, Appanaboyina S, Putman CM, Millan D, Frangi AF. Efficient pipeline for image-based patient-specific analysis of cerebral aneurysm hemodynamics: technique and sensitivity. *IEEE Transactions on Medical Imaging* 2005; **24**(1):457–467.
13. Taubin G. A signal processing approach to fair surface design. *Proceedings of the 22nd Annual Conference on Computer Graphics and Interactive Techniques (SIGGRAPH 1995)*, Los Angeles, CA, 1995.
14. Castro MA, Putman CM, Cebral JR. Computational fluid dynamics modeling of intracranial aneurysms: effects of parent artery segmentation on intra-aneurysmal hemodynamics. *AJNR American Journal of Neuroradiology* 2006; **27**:1703–1709.
15. Löhner R. *Applied CFD Techniques*. Wiley: New York, 2001.
16. Mut F, Aubry R, Löhner R, Cebral JR. Fast numerical solutions in patient-specific simulations of arterial models. *Communications in Numerical Methods in Engineering* 2009; DOI: 10.1002/cnm.1235.
17. Cebral JR, Castro MA, Soto O, Löhner R, Alperin N. Blood flow models of the circle of Willis from magnetic resonance data. *Journal of Engineering Mathematics* 2003; **47**(3–4):369–386.
18. Ford MD, Alperin N, Lee SH, Holdsworth DW, Steinman DA. Characterization of volumetric flow rate waveforms in the normal internal carotid and vertebral arteries. *Physiological Measurement* 2005; **26**:477–488.
19. Cebral JR, Castro MA, Putman CM, Alperin N. Flow-area relationship in internal carotid and vertebral arteries. *Physiological Measurement* 2008; **29**:585–594.
20. Taylor CA, Hughes TJR, Zarins CK. Finite element modeling of blood flow in arteries. *Computer Methods in Applied Mechanics and Engineering* 1998; **158**:155–196.
21. Castro MA, Putman CM, Cebral JR. Computational fluid dynamics modeling of intracranial aneurysms: effects of parent artery segmentation on intra-aneurysmal hemodynamics. *American Journal of Neuroradiology* 2006; **27**(8):1703–1709.
22. Jiang J, Strother CM. Computational fluid dynamics simulations of intracranial aneurysms at varying heart rates: a ‘patient-specific’ study. *Journal of Biomechanical Engineering* 2009; **131**(9):091001.
23. Löhner R, Appanaboyina S, Cebral JR. Parabolic recovery of boundary gradients. *Communications in Numerical Methods in Engineering* 2007; **24**:1611–1615.
24. Cebral JR, Löhner R. Distributed visualization in computational fluid dynamics. In *Computational Fluid Dynamics Review 1998*, Hafez M, Oshima K (eds). World Scientific: Singapore, 1998; 1097–1112.
25. Cebral JR, Mut F, Weir J, Putman CM. Association of hemodynamic characteristics and cerebral aneurysm rupture. *American Journal of Neuroradiology* 2010; DOI: 10.3174/ajnr.A2274.
26. Cebral JR, Castro MA, Burgess JE, Pergolizzi R, Sheridan MJ, Putman CM. Characterization of cerebral aneurysm for assessing risk of rupture using patient-specific computational hemodynamics models. *American Journal of Neuroradiology* 2005; **26**:2550–2559.
27. Cebral JR, Mut F, Weir J, Putman CM. Quantitative characterization of the hemodynamic environment in ruptured and unruptured brain aneurysms. *American Journal of Neuroradiology* 2010; submitted.
28. Ford MD, Hoi Y, Piccinelli M, Antiga L, Steinman DA. An objective approach to digital removal of saccular aneurysms: technique and applications. *The British Journal of Radiology* 2009; **82**, Spec No 1:55–61.
29. Piccinelli M, Veneziani A, Steinman DA, Remuzzi A, Antiga L. A framework for geometric analysis of vascular structures: application to cerebral aneurysms. *IEEE Transactions on Medical Imaging* 2009; **28**(8):1141–1155.
30. Griffith TM. Modulation of blood flow and tissue perfusion by endothelium-derived relaxing factor. *Experimental Physiology* 1994; **79**:873–913.
31. Moncada S, Plamer RMJ, Higgs EA. Nitric oxide: physiology, pathology and pharmacology. *Pharmacological Reviews* 1991; **43**:109–142.
32. Moritake K, Handa H, Hayashi K, Sato M. Experimental studies on intracranial aneurysms (a preliminary report): some biomechanical considerations on the wall structures of intracranial aneurysms and experimentally produced aneurysms. *No shinkei Sheka* 1973; **1**:115–123.
33. Sho E, Sho M, Singh TM, Xu C, Zarins C, Masuda H. Bloodflow decrease induces apoptosis of endothelial cells in previously dilated arteries resulting from chronic high blood flow. *Arteriosclerosis, Thrombosis and Vascular Biology* 2001; **21**:1139–1145.
34. Hara A, Yoshimi N, Mori H. Evidence for apoptosis in human intracranial aneurysms. *Neurological Research* 1998; **20**:127–130.
35. Fukuda S, Hashimoto N, Naritomi H, Nagata I, Nozaki K, Kondo S, Kurino M, Kikuchi H. Prevention of rat cerebral aneurysm formation by inhibition of nitric oxide synthase. *Circulation* 2000; **101**(21):2532–2538.
36. Nakatani H, Hashimoto N, Kang Y, Yamazoe N, Kikuchi H, Yamaguchi S, Niimi H. Cerebral blood flow patterns at major vessel bifurcations and aneurysms in rats. *Journal of Neurosurgery* 1991; **74**:258–262.
37. Perktold K, Peter R, Resch M. Pulsatile non-Newtonian blood flow simulation through a bifurcation with an aneurysm. *Biorheology* 1989; **26**(6):1011.
38. Oubel E, DeCraene M, Putman CM, Cebral JR, Frangi AF. Analysis of intracranial aneurysm wall motion and its effects on hemodynamic patterns. *SPIE Medical Imaging*, San Diego, CA, 2007.

39. Sforza D, Löhner R, Putman CM, Cebal JR. Hemodynamic analysis of intracranial aneurysms with moving parent arteries: basilar tip aneurysms. *International Journal for Numerical Methods in Engineering* 2010; **26**(10): 1219–1227.
40. Formaggia L, Nobile F, Quarteroni A, Veneziani A. Multiscale modeling of the circulatory system: a preliminary analysis. *Computing and Visualization in Science* 1999; **2**:75–83.